High-performance asymmetric supercapacitor based on vanadium dioxide/activated expanded graphite composite and carbon-vanadium oxynitride nanostructures

Ndeye M. Ndiaye [a,b], Ndeye F. Sylla [a,b], Balla D. Ngom [b], Farshad Barzegar [c], Damilola Momodu [a], and Ncholu Manyala [a]*

[a] Department of Physics, Institute of Applied Materials, SARChI Chair in Carbon Technology and Materials, University of Pretoria, Pretoria 0028, South Africa.

[b] Laboratoire de Photonique Quantique d'Energie et de NanoFabrication, Groupe de Physique du Solide et Science des Matériaux, Département de Physique FST-UCAD BP 5005 Dakar-Fan, Dakar, Sénégal

[c] Electrical, Electronic and Computer Engineering Department, University of Pretoria, Pretoria 0002, South Africa.

*Corresponding author email: ncholu.manyala@up.ac.za, Tel: + (27)12 420 3549;

Fax: + (27)12 420 2516

Highlights

- VO_2, VO_2/AEG composite and C-V_2NO materials were fabricated by CVD methods.
- VO_2/AEG displayed a higher electrochemical performance compared to VO_2 electrode.
- Asymmetric supercapacitor was assembled from VO_2/AEG and C-V_2NO as positive and negative electrodes respectively.
- The device exhibited a high specific energy and power of 41.6 Wh kg^{-1} and 904 W kg^{-1} respectively at 1 A g^{-1} in 1.8 V.

Graphical abstract

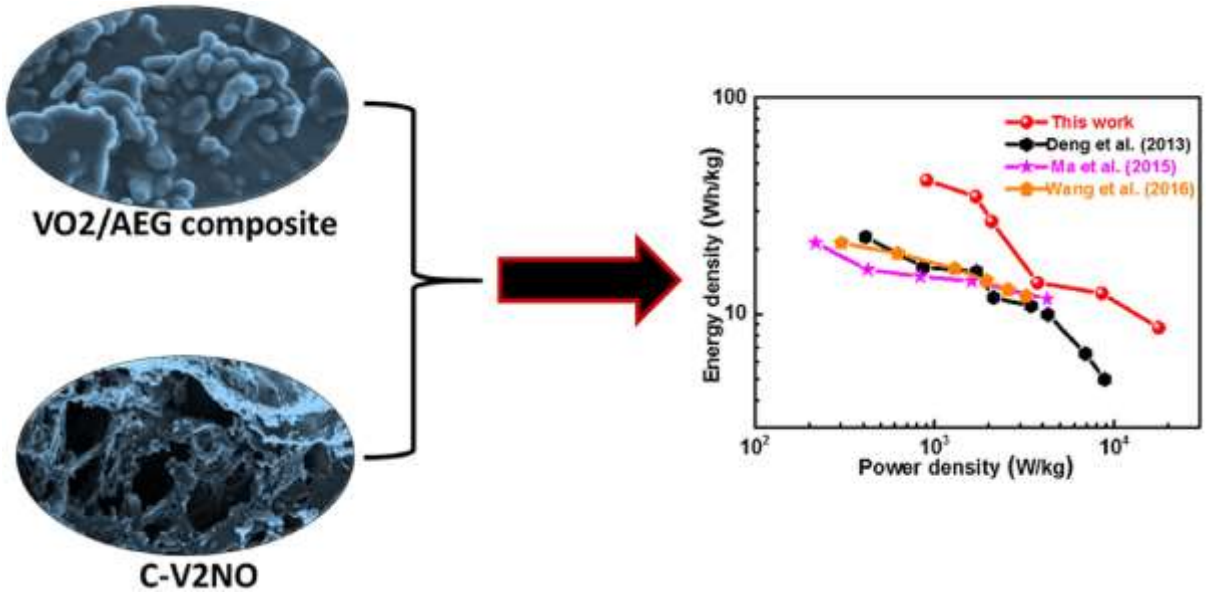

Abstract

The vanadium dioxide/activated expanded graphite (VO_2/AEG) composite and carbon-vanadium oxynitride (C-V_2NO) porous web-like structures were successfully synthesized by chemical vapor deposition (CVD) method. The X-ray diffraction analysis of the VO_2/AEG composite revealed the diffraction peaks of the monoclinic VO_2 and hexagonal AEG structures respectively while for the C-V_2NO material, a cubic crystal structure was observed. The Raman spectroscopy analysis of VO_2/AEG composite and C-V_2NO depicted vibration brands linked to vanadium dioxide with the distinct D, G, and D' peaks confirming the presence of disordered carbon into the main vanadium-based matrix. The electrochemical performance of the electrode material (VO_2/AEG//C-V_2NO) was evaluated in a two-electrode asymmetric device with the VO_2/AEG composite as the positive electrode and C-V_2NO as the negative electrode operating in a 6 M KOH electrolyte. The asymmetric device exhibited a specific energy of 41.6 Wh kg^{-1} with a corresponding specific power of 904 W kg^{-1} at a 1 A g^{-1} specific current in a large operating voltage of 1.8 V. The specific energy was still retained at 9 Wh kg^{-1} at an amplified specific current of 20 A g^{-1} with a specific power of 18 kW kg^{-1}. The supercapacitor showed a 93% capacity retention for up to 10,000 constant gravimetric current cyclic stability test at a specific current of 10 A g^{-1} with a good rate capability. A notable device stability was maintained without any failure via voltage floating tests for up to 100 h.

Keywords: Asymmetric supercapacitor, VO_2, AEG, Composite, C-V_2NO.

1. Introduction

Supercapacitors also known as electrochemical capacitors (ECs) have been known to be great candidates for the future generation of energy storage [1–3]. ECs are high power devices which can store and deliver energy relatively faster than batteries [4]. Currently, the spotlight is on these devices due to their application merits which include their high power density, long cycle life and safety [5]. Although supercapacitors still suffer low energy density as compared to batteries [6], they have higher energy density than conventional capacitors.[7–9].

Generally, supercapacitors are mainly classified into three classes based on their energy storage mechanism; the Electrochemical Double Layer Capacitors (EDLCs) are the first class which

arise from the accumulation of charges at the electrode/electrolyte interface [6]. EDLC storage behavior is mainly exhibited in carbon-based materials. The pseudocapacitors and faradaic capacitors are next class which are governed by a chain of Faradaic reactions which store the charges via redox reactions. Common materials in this class of supercapacitors include transition metal oxides, hydroxides (TMOs/TM-OHs) and redox polymers. Lastly, the hybrid capacitors that are considered as a combination of both EDLC and Faradaic materials [10]. In this storage category, the materials usually exist combined mechanisms as either a composite material or separate individual electrodes in non-symmetric device architecture. The positive electrode is composed of metal oxides/hydroxide [11–14] and conductive polymers [15,16] that give higher specific capacity [8,10] than the negative electrode which is usually made up of EDLC consisting of carbon-based materials. Activated carbon (AC) [17,18], carbon nanotubes (CNT) [19], graphene [20,21] and carbon nitride/oxynitride-based nanostructures are examples of materials which have been successfully used in these devices [22–24]. These carbon nanomaterials possess high specific surface area, good electronic conductivity, and long cycle stability [25–27] as compared to faradaic materials.

Asymmetric capacitors (AsyCs) are considered as a subclass of hybrid capacitors obtained by combining two different materials as a positive and an negative electrodes in the same cell. AsyCs are considered as a promising candidate and reliable approach to maximizing the specific capacitance and to extend the cell potential in order to improve the energy density [28].

Among all transition metal oxides, vanadium oxides family such as vanadium dioxide (VO_2) vanadium pentoxide (V_2O_5) and divanadium trioxide V_2O_3 have received great consideration in energy storage devices [29–38] due to their multiple oxidation states, low cost and non-toxic chemical properties [39,40]. In addition Vanadium dioxide (VO_2) has been largely studied as a potential electrode material in ECs due to its structural stability [39] and excellent reactivity [41]. However, as all metal oxides, VO_2 also displays a poor electrical conductivity and cyclic

stability as compared to carbon-based materials [42]. Numerous scholars have studied different methods with an aim to improve the electrochemical performance of the VO_2 materials. For instance, the synthesis of carbon/VO_2 composite materials such as graphene/VO_2 [39], VO_2/ CNTs [40] and VO_2@PANi [43] have been recently explored as an electrodes for electrochemical capacitors. Carbon/VO_2 composites have been demonstrated as suitable electrode materials to enhance the electrochemical properties of supercapacitors owing to their synergistic properties but most studies focus on either the positive electrode or negative electrode alone. For instance, Chen *et al*. [44] assembled an asymmetric supercapacitors by considering a CNT/V_2O_5 nanowire composite as a negative electrode and AC as a positive electrode in an organic electrolyte. The asymmetric capacitor showed a specific energy of 40 W h kg^{-1} at a power density of 210 W kg^{-1} at 0.5 mA cm^{-2} [44]. Recently, Zhou *et al*. [45] fabricated an asymmetric device where a bamboo-like V_2O_5/polyindole@activated carbon cloth (V_2O_5/PIn@ACC) was used as a positive electrode whereas a reduced graphene oxide@activated carbon cloth (rGO@ACC) was employed as a negative electrode.

The asymmetric capacitor displayed a specific energy of 38.7 W h kg^{-1} at the power density of 900 W kg^{-1} by using a specific current of 1 A g^{-1} [45]. Fleischmann *et al*. [46] successfully fabricated an asymmetric capacitor by using an AC as a positive electrode and vanadium oxide/carbon onion (VO_2/OLC) composite as a negative electrode with 1 M $LiClO_4$ in acetonitrile (ACN) electrolyte. The asymmetric device exhibited a specific energy of 45 W h kg^{-1} and a specific power of 58 kW kg^{-1} at 0.05 A g^{-1} [46]. Similarly, Hosseini *et al*. [47] assembled an asymmetric device by adopting a VO_2 nanosheet array grown on porous carbon nanofibers (VO_2@PCNFs) as a positive electrode and a porous carbon nanofibers (PCNFs) as a negative electrode in Na_2SO_4–poly(vinyl alcohol) (Na_2SO_4/PVA) gel electrolyte. The asymmetric capacitor displayed a specific energy of 75.06 W h kg^{-1} and a specific power of 1.275 kW kg^{-1} at a specific current of 1 Ag^{-1} [47]. No studies have considered the use of

vanadium oxides/carbon composites in both electrodes for an asymmetric design with the idea of harnessing both the porosity and conductivity known to carbon-based materials.

In this paper, we report a novel design of a vanadium dioxide/activated expanded graphite composite (VO_2/AEG) and carbon-vanadium oxynitride (C-V_2NO) porous web-like structures produced by the CVD method. The outstanding electrochemical performance of porous AEG reported in our previous work [48] inspired its introduction into the VO_2 main frame to create a good interaction between VO_2 and AEG using a facile method.

On the other hand, the C-V_2NO displayed a specific surface area value of 121.6 m^2 g^{-1} and a unique morphology with irregular porous cavities which could deliver a good electrochemical performance in supercapacitors. An AsyC was assembled by combining the merits of both materials based on VO_2/AEG composite as a positive electrode and C-V_2NO as a negative. The device displayed high specific energy of 41.6 W h kg^{-1} associated with a specific power of 904 W kg^{-1} at a specific current of 1 A g^{-1} and capacity retention of 93% up to 10,000 cycles.

2. Experimental

Ammonium metavanadate (NH_4VO_3, purity 99 %), Melamine ($C_3H_6N_6$, purity 99 %), Hydrochloric acid (HCl, 37% AR grade) and 10 wt% Polyvinylpyrrolidone (PVP) were purchased from Sigma-Aldrich and used without further purification. Polycrystalline Nickel foam (NiF) (3D scaffold template with an areal density of 420 g m^{-2} and a thickness of 1.6 mm was purchased from Alantum (Munich, Germany). Potassium hydroxide (KOH, min 85%) was purchased from Merck (South Africa). Graphite grade ES 250 B5 was obtained from Qingdao Kropfmuehl Graphite of 10 wt%.

2.1 Synthesis technique

2.1.1 Synthesis of AEG and VO_2 materials

Activated expanded graphite (AEG) was prepared from the expanded graphite (EG) using a microwave-assisted method. The EG was carbonized by using a CVD method at 800 °C under argon and hydrogen for 2h to obtain the final product. The detailed description of AEG is previously reported by Barzegar *et. al*. [48]. The vanadium dioxide (VO_2) was synthesized by a temperature CVD-assisted route at 900 °C for 2 h under nitrogen (N_2) atmosphere. The detailed description of VO_2 is presented in the report by Ma *et al.* [49].

2.1.2 Synthesis of VO_2/AEG composite

The VO_2/AEG composite was prepared by simply mixing 1.8 g of NH_4VO_3 and 90 mg of AEG in an agate mortar. The mixture was inserted into a quartz tube furnace and heated to 900 °C at a heating rate of 2 °C min^{-1} and kept at that temperature for 2 h under nitrogen (N_2) atmosphere. After cooling down to room temperature under a flow of nitrogen, the resulting black powder was ground in an agate mortar to obtain the final product.

2.1.3 Synthesis of C-V_2NO nanostructures

The C-V_2NO was synthesized following a similar process as that of the VO_2/AEG composite as follows: 0.5 g of NH_4VO_3 and 5 g of $C_3H_6N_6$ were mixed in an agate mortar with a few drops of ethanol to make a homogeneous slurry. The slurry was subsequently calcined in a tube furnace from room temperature to 800 °C at a heating rate of 18 °C min^{-1} and left to dwell at this temperature for 2 h under nitrogen (N_2) atmosphere. After naturally cooling down, the final carbon-vanadium oxynitride product was obtained.

2.2 Structural and Morphological characterization

The X-ray diffraction (XRD) patterns for the VO_2/AEG composite and the C-V_2NO materials were recorded using a XPERT-PRO diffractometer (PANalytical BV, Netherlands, CoKα (λ= 0.178901 nm) radiation) with 2θ values ranging from 10° – 90°. The Raman spectroscopy measurements of the materials were studied using a WITec confocal Raman microscope (WITec alpha300 R, Ulm Germany) with a 532 nm laser wavelength and a spectral acquisition time of 60 s. The Raman system laser power was set as low as 5 mW in order to minimize heating effects. The porosimetry test of the materials was evaluated with a nitrogen adsorption–desorption isotherms at -196°C using a Micromeritics ASAP 2020. The specific surface area of the materials were evaluated by the Brunauer–Emmett–Teller (BET) analysis from the adsorption branch in the relative pressure range (P/P0) of 0.01–1.0. The morphology and the element distribution mapping of the composite and the carbon-vanadium oxynitride were characterized using a high-resolution Zeiss Ultra plus 55 field emission scanning electron microscope (FE-SEM), operated at a voltage of 2.0 kV and a JEOL JEM-2100F high resolution transition electron microscope (HRTEM) at 200 kV. The X-ray photoelectron spectroscopy (XPS, K-alpha, Thermo Fisher) was used to analyse the elemental composition of the materials with a monochromatic Al-Kα radiation.

2.3 Electrodes preparation and electrochemical characterization

The VO_2, VO_2/AEG composite and carbon-vanadium oxynitride electrodes were prepared by mixing 80 wt% of the active material with 10 wt% of carbon black (as conducting additive) and 10 wt% of polyvinylidene difluoride (PVDF) binder in an agate mortar. The mixture was then dissolved with a few drops of 1-methyl-2-pyrrolidinone (NMP) to form a slurry which was coated onto NiF current collectors with an area of 1×1 cm^2. The electrodes were dried at 60 °C for 12 hours to ensure complete evaporation of the NMP.

The electrochemical properties of the VO_2, VO_2/AEG composite and C-V_2NO electrodes were evaluated using a Bio-Logic VMP-300 (Knoxville TN 37,930, USA) controlled by the EC-lab V 11.40 software in a three (half-cell) electrode configuration. Ag/AgCl (KCl saturated) as reference electrode, a glassy carbon plate as counter electrode and VO_2/AEG composite and C-V_2NO electrodes as working electrodes were used to investigate the electrochemical measurements in a 6 M KOH aqueous electrolyte.

The asymmetric device was fabricated using VO_2/AEG composite as a positive and C-V_2NO as a negative electrodes respectively in 6 M KOH electrolyte. The VO_2/AEG//C-V_2NO was assembled in a Swagelok cell with a microfiber filter paper as a separator.

The cyclic voltammetry (CV) measurements were carried out to determine the behaviour of the VO_2/AEG and C-V_2NO electrodes and their ideal working potential in three- and -two configurations cell. The galvanostatic charge-discharge (GCD) measurements aid to obtain the specific capacity and the stability test of the VO_2/AEG and C-V_2NO electrodes

The electrochemical impedance electrochemical test was used to investigate the capacitive properties and conductivity of the VO_2/AEG and C-V_2NO electrodes in the frequency range of 100 kHz–10 mHz in open circuit voltage. All the electrochemical tests were performed at room temperature.

2.3.1 Structural and morphological properties

X-ray diffraction (XRD) analysis results of VO_2/AEG composite and C-V_2NO materials are presented in Fig. 1. The XRD patterns of VO_2/AEG composite (Fig. 1(a)) showed diffraction peaks of the VO_2 and AEG materials confirming a stable composite of AEG with the VO_2 material.

The XRD patterns of the VO_2 material can be indexed to a VO_2 monoclinic structure (black indices in the figure 1(a)) with a *P1 2_1/c(14)* space group and lattice parameters; a = 5.3532 Å,

b = 4.5380 Å, c = 5.3830 Å, and β = 115.2° using the matching inorganic crystal structure database (ICSD) card #4033. However, Fig. 1(a) also shows a satellite peaks located at 17.6 ˚ and 20.5 ˚which correspond to trace amounts of V_6O_{13} [48]. The diffraction peaks of the AEG in Fig. 1(a) exhibited a hexagonal structure which can be indexed to the (002), (100), (101), (102), (004) and (103) planes of the graphite labelled blue in the figure, with a *P63/mmc* space group. The lattice parameters in this case were given as a = 2.4704 Å, b = 2.4704 Å, c = 6.7244 Å, γ = 120.0° using the matching inorganic crystal structure database (ICSD) card #1487.

In Fig. 1(b), the XRD patterns of C-V_2NO were indexed to a cubic structure with a single phase with the diffraction peaks corresponding to (111), (200) and (220). An *Fm-3m(225)* space group with lattice parameters a = 4.1313(1) Å, a/b = 1.0000, b/c = 1.0000 and c/a = 1.0000 was obtained with the matching inorganic crystal structure Database (ICSD) card # 43182.

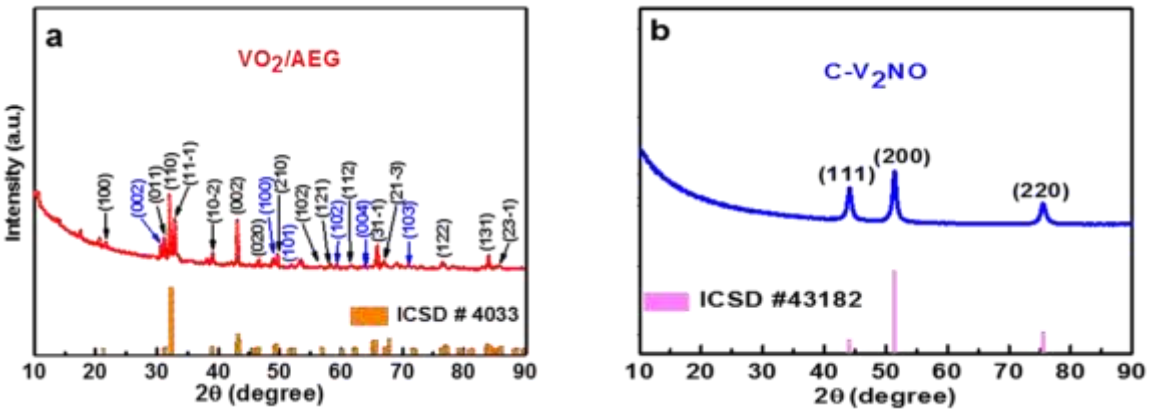

Fig. 1: The XRD patterns of (a) VO_2/AEG composite (with black and blue indexes for VO_2 and AEG (carbon peaks) respectively) and (b) C-V_2NO nanostructures

.

The Raman spectroscopy of the VO_2/AEG composite and C-V_2NO materials were used to identify different phases at the molecular level.

The Raman vibrational modes of the VO_2 material are located at 139, 194, 287, 410, 527, 688 and 1000 cm^{-1} wavenumbers as shown in Fig. 2(a). At wavenumber ranging from 100 – 400

cm^{-1}, the V–O−V bending modes are observed. At 400 – 800 cm^{-1} wavenumber range, the bands recorded are attributed to the V–O−V stretching modes. The Raman bands located at 800 – 1100 cm^{-1}, are attributed to the V=O stretching modes which are linked to the monoclinic VO_2 (M) [50–52]. The Raman vibrational modes of the VO_2 material have have been assigned to well-known vibrational modes of the material except for the 527 cm^{-1} (B_g species) as shown in Table. 1 [53]. The band at 1000 cm^{-1} is attributed to the stretching of the V=O arising from the typical bands of V_2O_5. This revealed the presence of the V_2O_5 in the composite material [54].

Fig. 2(a) also shows three peaks at 1349, 1583 and 2710 cm^{-1} which are attributed to the D-band (linked to defects or the disorders present in the carbon lattice structure [55,56]), G-band (carbon-carbon vibration mode [55,57]) and the 2D-band (originating from the double resonance process) band of AEG, respectively [48]. All these confirm the presence of both AEG and VO_2 materials in the composite.

Table. 1: Raman modes of VO_2 [53].

Raman frequency (cm^{-1})	Vibration assignment
139	A_g
194	A_g
287	A_g
410	A_g
527	B_g
688	A_g

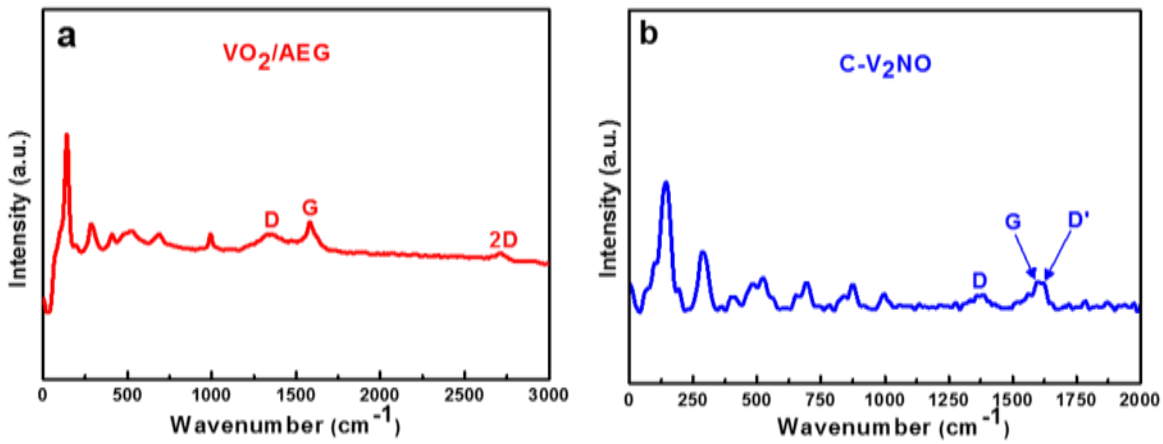

Fig. 2: The Raman spectra of the (a) VO_2/AEG composite and (b) C-V_2NO nanostructures.

In Fig. 2(b), the Raman bands indicated that different vanadium species are formed during the growth of the carbon-vanadium oxynitride materials. For instance, the Raman bands at 145, 285 and 479 cm^{-1} confirm the existence of V_2O_5 and VO_2 respectively, in the metal oxynitride–carbon. The high-intensity peak at 142 cm^{-1} wavenumbers is linked to the bending vibration (B_{3g} species) associated with the layered structure [58]. The Raman band located at 285 cm^{-1} is due to the bending vibrations of O-V-O bond (B_{2g} mode) while for the 479 cm^{-1} is attributed to the stretching of the V–O−V (B_g) [59–61]. In addition, these two high intensities peaks at 145 cm^{-1} and 285 cm^{-1} could be associated with the cubic symmetry of the vanadium oxynitride [62].

However, it also showed a D peak at 1373 cm^{-1}, G peak at 1593 cm^{-1} and D'-peak at 1621 cm^{-1}. The D'-peak observed near the G peak showed that the carbon present in the C-V_2NO is a graphene-like carbon. The D' peak is attributed to the lattice vibration of the G band but mainly due to the graphene layers at the surface of the carbon material present in the material [48,63]. The presence of the three peaks (D, G, and D') confirmed the presence of the carbon element in the as-prepared carbon-vanadium oxynitride.

The specific surface area of the VO_2, VO_2/AEG composite and the C-V_2NO materials were determined by the BET method. Fig. 3 and Fig. S1 display the nitrogen adsorption-desorption isotherm of the materials.

In Fig. 3a and Fig.S1, a type III isotherm with an H3 hysteresis loop was depicted for the VO_2 and VO_2/AEG composite which indicated a weak interaction between the N_2 adsorbent and the material. The C-V_2NO in Fig. 3(b) shows a type IV isotherm with H3 hysteresis which is indicative of a mesoporous structure. These hysteresis behaviour of the materials indicated non-rigid aggregates of plate-like particles or assemblages of slit-shaped pores [64]. The specific surface areas (SSA) recorded for VO_2, VO_2/AEG composite and the C-V_2NO materials were 1.5 m^2 g^{-1}, 4.6 m^2 g^{-1} and 121.6 m^2 g^{-1}, respectively.

As compared to VO_2, the high SSA of VO_2/AEG composite can be attributed to the presence of AEG in the network VO_2 which could facilitate the formation of polycrystalline islands and channels. For the C-V_2NO material, the value of the SSA is higher as compared to other vanadium-based oxynitride materials [65,66] which could be associated to the mesoporous structure.

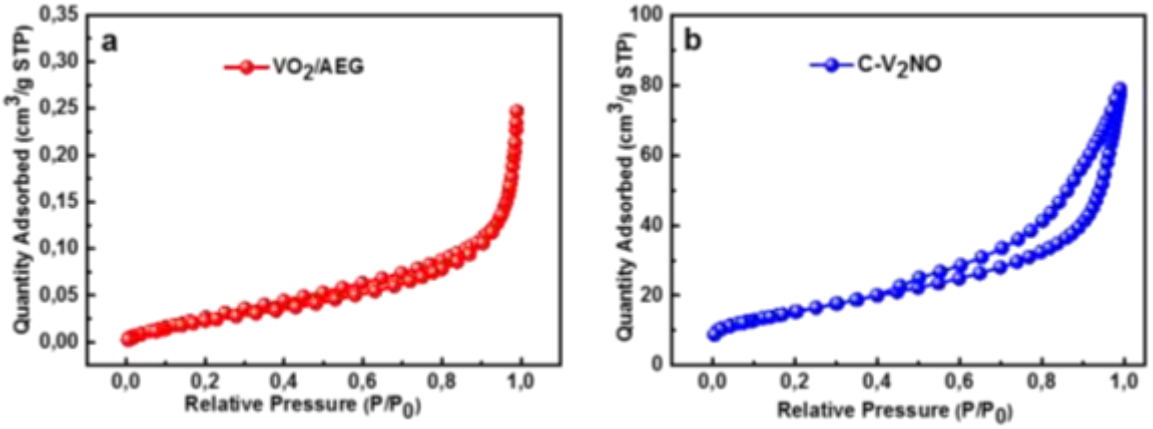

Fig. 3: The N_2 absorption/desorption isotherms of (a) VO_2/AEG composite and (b) C-V_2NO nanostructures.

The morphology analysis of the VO_2/AEG composite and C-V_2NO materials is presented in Fig. 4 by scanning electron microscopy (SEM). The SEM micrograph of the pristine VO_2 sample revealed a rod morphology with an agglomerated particles (Fig. S2).

Fig. 4(a) shows the network of an interconnected sheet-like structure of the AEG [48] and the structure of VO_2, respectively. Fig. 4(b) presents the SEM morphology of the VO_2/AEG composite which displays clearly the VO_2 rods grown on the surface of the activated expanded graphite (AEG) sheet-like structure. The VO_2 rods on the surface of the AEG showed a non-uniform structure with an agglomerated rods. The distribution of the VO_2 rods on the AEG surface leads to an enhanced interaction which maximizes the electrochemically accessible area that yields a good electrochemical performance in supercapacitors by providing efficient channels for charge and ionic transport.

The morphology of the C-V_2NO in Figs. 3(c-d) showed a web-like structure with irregular porous cavities. As seen, the surface morphology of the C-V_2NO showed the agglomeration of porous granular with an interconnected network with cavities to form a web-like structure which aids electrolyte efficient penetration [67].

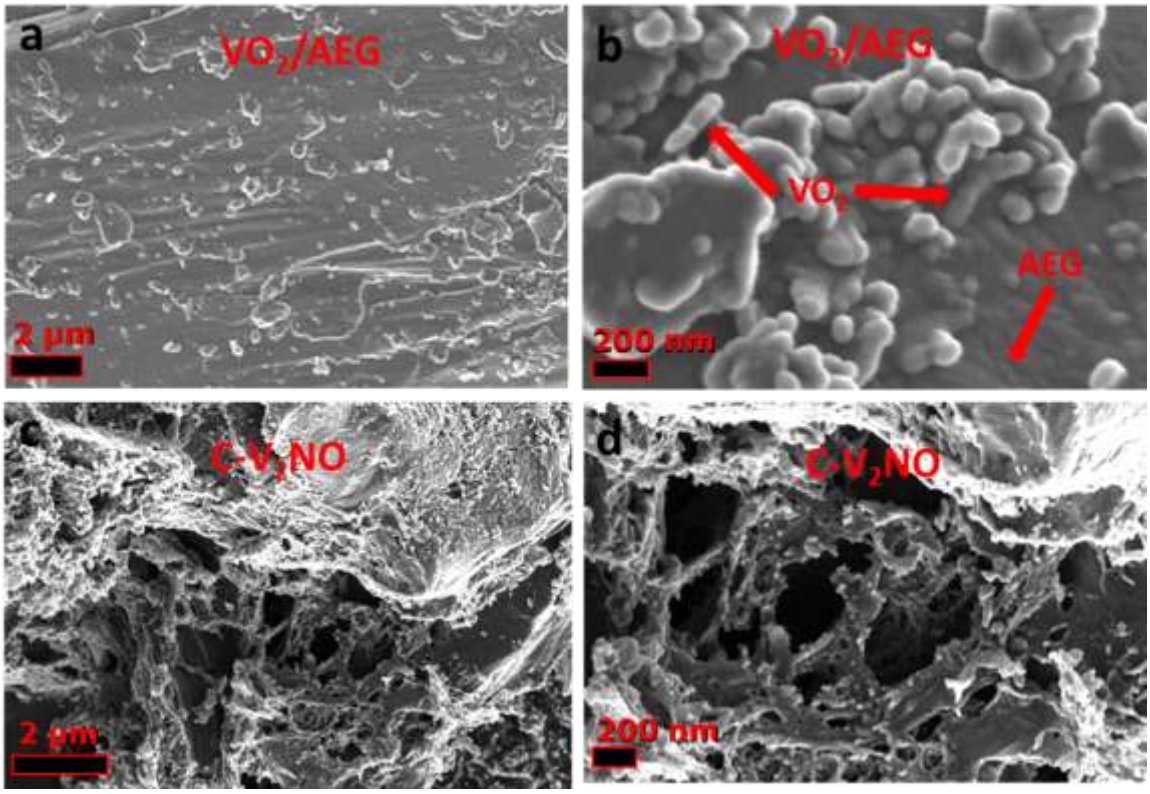

Fig. 4: The SEM images of the as-synthesized (a - b) VO_2/AEG composite and (c - d) C-V_2NO nanostructures.

Fig.5 presented the element distribution mapping of the composite and the web-like C-V_2NO nanostructures. It displayed the presence of V, C and O atoms in the VO_2/AEG composite while for the C-V_2NO, shows V, C, O, and N atoms in the materials. The Fig. 5(a - d) clearly indicates that all the elements in these composites are uniformly distributed.

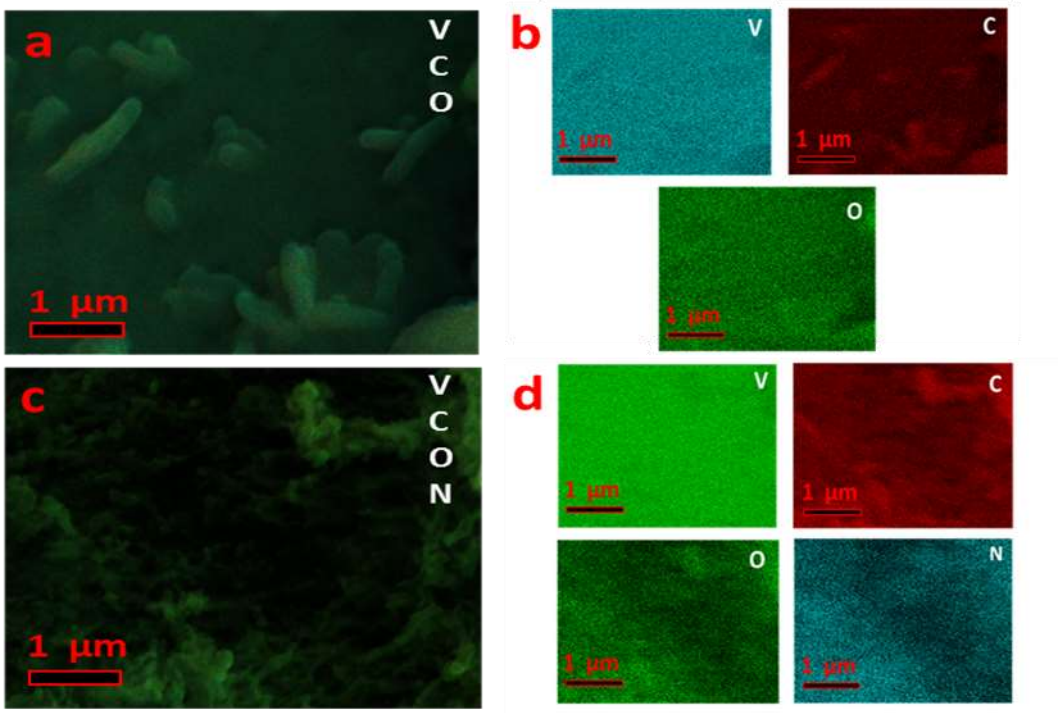

Fig. 5: (a) VO_2/AEG composite elemental mapping, (b) distribution of individual elements in the VO_2/AEG composite, (c) C-V_2NO elemental mapping and (d) distribution of individual elements in the C-V_2NO.

The TEM images were further used to study the morphology of the VO_2/AEG composite and C-V_2NO materials in Fig. 6. The TEM micrograph of the VO_2/AEG composite in Fig. 6(a) shows an overlapping of the AEG sheet-like structure and the rods morphology of VO_2(M). The VO_2(M) rods are verified by using high-resolution TEM (inset to Fig. 6(a)). The HRTEM revealed the crystallinity structure of the VO_2(M) with clear lattice fringes. The interplanar spacing is~ 3.3 Å which corresponded to the (011) lattice planes, further confirming the existence in VO_2 (M) in the composite material [68].

In Fig. 6(b), the micrograph of the C-V_2NO at low and high magnification (inset to Fig. 6(b)) showed clearly the presence of the porous structure which confirms the observations from SEM analysis.

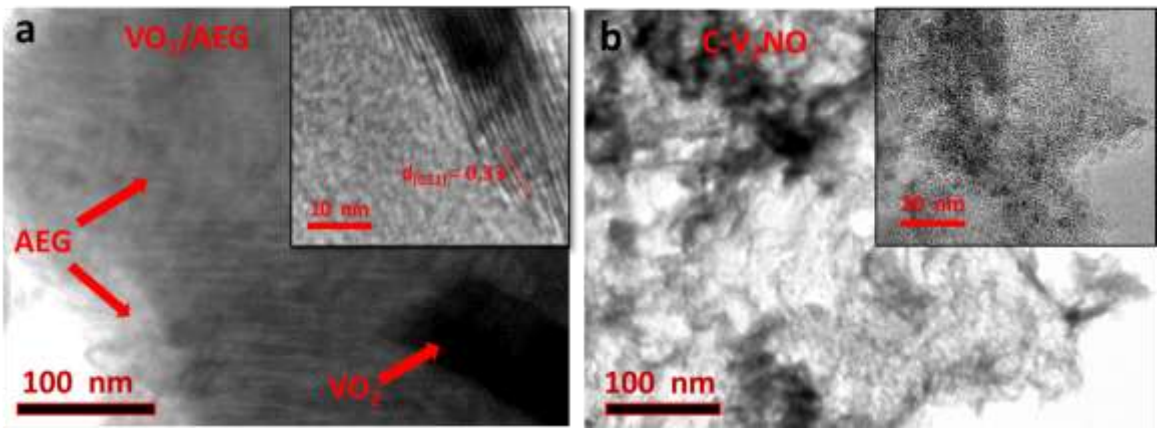

Fig. 6: The TEM images of the synthesized (a) VO_2/AEG composite (the inset is the HRTEM of the composite material) and (c) C-V_2NO nanostructures (the inset shows the HRTEM).

The surface characterization of both materials was further investigated by using the X-ray photoelectron spectroscopy (XPS) as shown in Fig. 7. The chemical states of both materials are quantitatively evaluated to determine the amount of active vanadium, nitrogen, oxygen and carbon content in the materials. Figs. 7(a) and (b) display the wide scan XPS spectrum of the as-received VO_2/AEG composite and C-V_2NO@800 °C materials respectively.

The core level of V*2p*$_{3/2}$ from the VO_2/AEG composite exhibited three peaks as shown in Fig. 7(c). The high binding energy at 516.5 eV suggests that the oxidation state of the composite is predominantly V^{4+} which confirm the formation of VO_2 [69]. The other peaks located at 516.9 eV and 517.7 eV were attributed to the mixed-valence of the vanadium ions (V^{4+} and V^{5+} respectively) of the satellite V_6O_{13} [70,71]. The XPS spectrum clearly shows that the phase synthesized herein is VO_2 with a trace presence of V_6O_{13}.

In Fig. S3, the XPS signal of the N1s from the C-V_2NO@800 °C was deconvoluted into a three peak Gaussian components. The peak at 397.3 eV binding energy value was attributed to N from vanadium nitride. The other two peaks at 399.4 eV and 400.5 eV were assigned to the pyrrolic-N and graphitic-N, respectively.

The V$2p_{3/2}$ binding energies of the C-V_2NO@800 °C is presented in Fig. 7(d). The core level of V$2p_{3/2}$ reveals four peaks located at 513.7 eV, 515.5 eV, 516.5 eV and 517.7 eV which are ascribed to the vanadium ions V^{2+}, V^{3+}, V^{4+} and V^{5+} respectively [72,73].

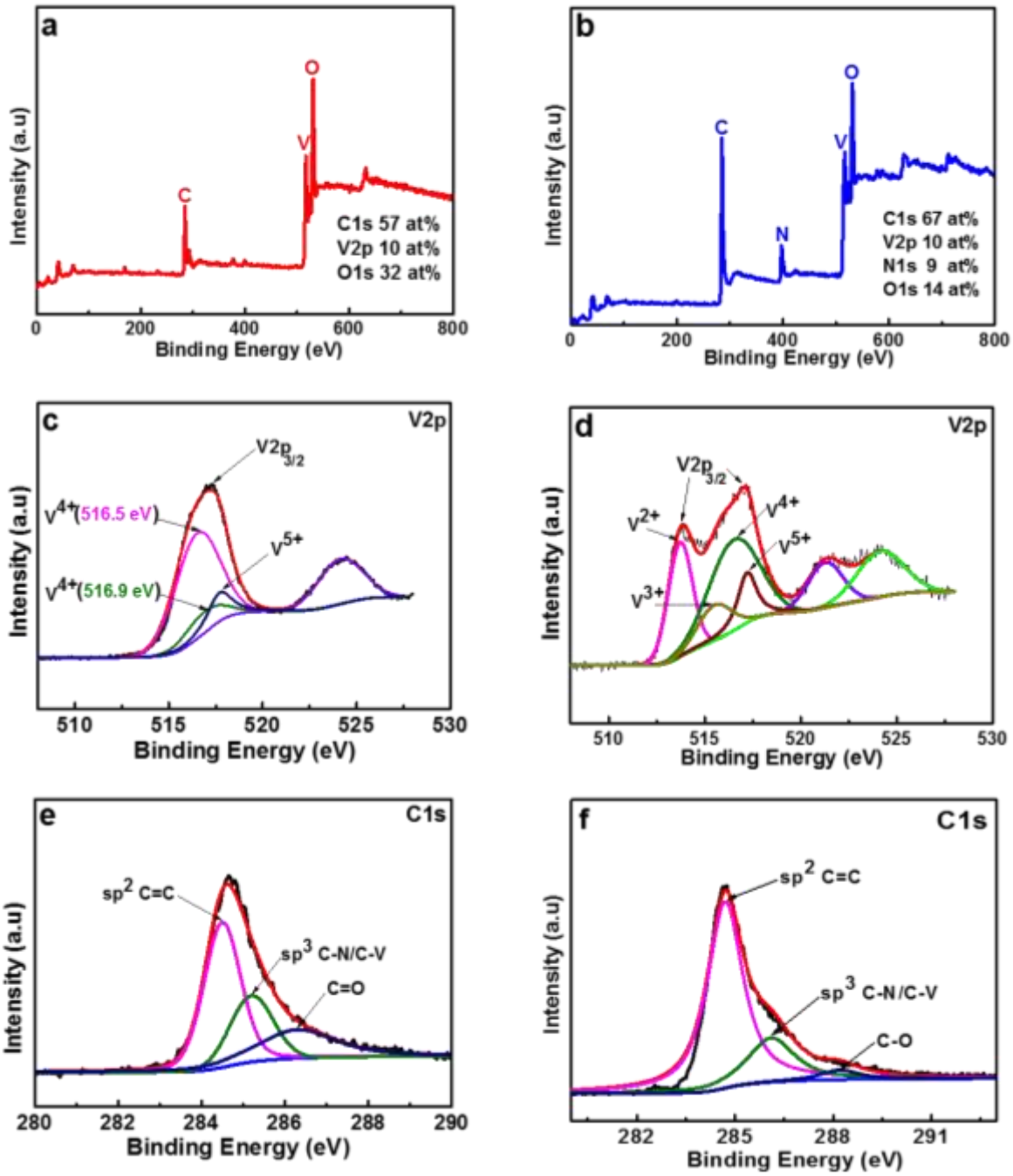

Fig. 7: The wide scan XPS spectrum of the as- received (i.e., without sputter cleaning) of (a) VO_2/AEG composite and (b) C-V_2NO@800 °C. The fitted core level spectrum of V2p from (c) VO_2/AEG composite and (d) C-V_2NO@800 °C. The core level spectra of C1s from (e) VO_2/AEG composite and (f) C-V_2NO@800 °C.

Fig. 7(e) and (f) show the fitted core level spectrum of C1s of both materials. The high binding energy peaks of VO_2/AEG composite (at 284.4 eV) and C-V_2NO@800 °C (at 284.6 eV) correspond to the sp^2 C = C bond which confirms the predominant content of graphitic carbon in the material [74,75]. The peaks located at 285.2 eV for VO_2/AEG composite and 285.5 eV for C-V_2NO@800 °C were ascribed to the carbon (C) sp^3 linked to the nitrogen (N) or the vanadium (V) atoms [76,77]. The low binding energy peaks of VO_2/AEG composite (at 286.3 eV) and C-V_2NO@800 °C (at 288.2 eV) are attributed to the sp^3 C-O bonding structures [78,79].

2.3.2 Electrochemical performances of VO_2/AEG//C-V_2NO

2.3.2.1 Electrochemistry of the VO_2/AEG and C-V_2NO

Electrochemistry involves charge transfer between two electrodes (positive and negative electrodes), and an interconnecting electrolyte [80]. The chemical reaction arises at the electrode/electrolyte interface which can either be driven by electrical energy or yield electrical energy. The electrode materials in electrochemistry must have the ability to possess high electronic conductivity while the electrolyte should have a low electronic conductivity with high ionic conductivity [81]. A typical design to realize the electrochemical measurements is by using a so-called three (3)-electrode configuration setup. It is adopted to minimize the energy lost in the system by reducing the distance between the components [82]. Generally, the operation of electrochemical capacitors is determined by the type of electrode material used. In this work, faradaic materials were used and thus, the mode of charge storage was based on redox reactions. All the electrochemical measurements were evaluated in 6 M KOH with a high ionic conductivity (i.e. 73.5 and 198 Scm^2mol^{-1} for K^+ and OH^-, respectively [83]), and VO_2, VO_2/AEG and C-V_2NO were used as electrode materials. The mechanism reaction of the VO_2 electrode in 6 M KOH is based on this equation:

$$VO_2 + OH^- \leftrightarrow VO_2(OH) + e^- \quad (1)$$

The VO_2/AEG and C-V_2NO materials have higher electronic conductivities than the VO_2 sample. This is linked to the presence of carbon in the materials which could increase the specific surface area enhancing the electrochemical performance of the VO_2 materials.

2.3.3 Three (3)-electrode configuration of the VO_2/AEG composite and C-V_2NO electrodes

In three electrode configuration, the electrochemical measurements of the VO_2/AEG composite and C-V_2NO electrodes were evaluated using 6 M KOH as an aqueous electrolyte.

As seen in Fig. S4 (supporting information), the VO_2/AEG composite exhibited higher current response and specific capacity as a function of the specific current than the pristine material. It also showed a better coulombic efficiency (99%) as compared to the VO_2 electrode with 97% coulombic efficiency up to 5000 cycles at 10 A g^{-1}.

Thus, the VO_2/AEG composite shows the best electrochemical performance as compared to the VO_2 electrode. This is due to the strong synergy between the two materials where AEG improves both good electrical conductivity and high specific surface area to VO_2, but has much high specific capacity as being oxide material as compared AEG carbon material.

Fig. 8 shows the individual electrochemical performance of both electrode materials. The cyclic voltammograms (CV) curves of the VO_2/AEG composite electrode were shown in Fig. 8(a) at scan rates ranging from 5 to 100 mV s^{-1} within a potential window range of 0.0 - 0.5 V. The curves exhibits reduction and oxidation peaks related to the electrochemical redox reactions at the electrode/electrolyte interface. The CV curves reveal the conventional behavior of a faradaic-type electrode.

The CV curves of the C-V_2NO electrode were shown in Fig. 8(b) at different scan rates from 5 to 100 mV s^{-1} in a negative potential window range of -1.2 V to 0.0 V. The CV curve at 50 mV s^{-1} displayed a two-pairs of redox peaks corresponding to the anodic peaks at -0.80 V and -0.38 V and cathodic peaks at -0.87 V and -0.53 V, respectively. Mostly, two pairs of broad

redox peaks in the CV curve could be related to M–O/M–O–OH, in which M is V in this work [84].

As observed, the reversibility of these redox reactions confirmed the pseudo-capacitive behavior. The high electrochemical property of the C-V_2NO web-like nanostructure can be ascribed to the unique porous morphology architecture and the conductivity of the materials.

In Fig. 8(c), the corresponding galvanostatic charge discharge (GCD) curves of the electrode at different specific currents in the potential window of 0.0 to 0.5 V is displayed for VO_2/AEG composite. Each GCD curve showed a non-linear profile confirming the faradic behavior of the VO_2/AEG composite electrode.

The GCD curves of the C-V_2NO electrode shown in Fig. 8(d) present the existence of a faradaic behavior as seen in the CV plots for different specific currents.

Based on the GCD curves of VO_2/AEG and C-V_2NO electrodes, the specific capacity Q (mA h g^{-1}) was calculated using equation 2;

$$Q = \frac{I_d \times t_D}{3.6} \tag{2}$$

where I_d is the gravimetric specific current in A g^{-1}, t_D is the discharge time (s), and Q is the specific capacity (mA h g^{-1}).

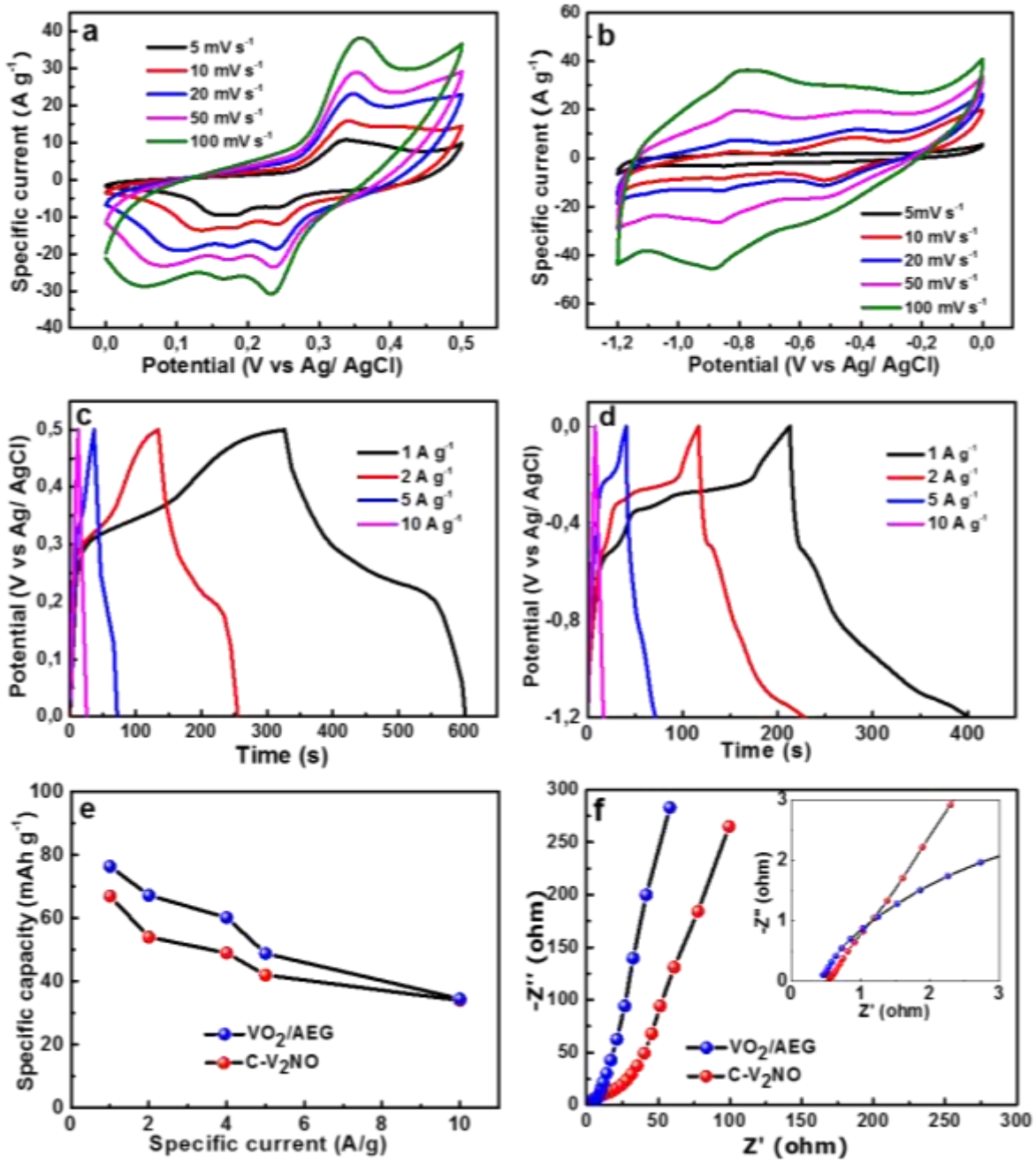

Fig. 8: CV curves of the (a) VO_2/AEG composite and (b) C-V_2NO materials at different scan rates respectively. GCD profile of the (c) VO_2/AEG composite and (d) C-V_2NO at different specific currents respectively. (e) specific capacities for VO_2/AEG composite and C-V_2NO as a function of the specific current and (f) Nyquist plots of VO_2/AEG composite and C-V_2NO electrode materials.

Fig. 8(e) displays the calculated specific capacities of both electrodes at different specific currents. The specific capacities of the VO_2/AEG composite and C-V_2NO electrodes reach 76 and 67 mA h g^{-1}, respectively at a specific current of 1 A g^{-1}.

These high specific capacity values of the VO_2/AEG and C-V_2NO electrodes are linked to the presence of carbon in both oxides materials, which improves the electrical conductivity of both VO_2/AEG composite and C-V_2NO materials.

Fig. 8(f) displayed the Nyquist plot of the VO_2/AEG composite and C-V_2NO samples at a frequency ranging from 100 kHz-10 mHz. As seen, the Nyquist plot of the VO_2/AEG composite presents a slight deviation from the vertical line. The equivalent series resistance (ESR) values for the VO_2/AEG and the C-V_2NO electrodes were 0.42 Ω and of 0.54 Ω, respectively. These low ESR values indicate a good electrolyte/electrode interface interaction and a low contact resistance between the current collector and the electrodes materials [85].

2.3.4. Two (2)-electrode configuration of the asymmetric device

To evaluate entirely the electrochemical performance of the VO_2/AEG composite and C-V_2NO electrodes, an asymmetric device was assembled using VO_2/AEG composite as a positive and C-V_2NO as a negative electrodes respectively in 6 M KOH.

Based on the difference in specific capacities of VO_2/AEG composite and C-V_2NO electrodes in Fig. 8(e), a charge balance ($Q_{VO_2/AEG} = Q_{V_2NO-C}$) is necessary for the asymmetric cell. The masses of both electrodes were calculated by using the following equations (3) and (4) with Q being the specific capacity as per equation 2:

$$Q_{VO_2/AEG} = Q_{C-V_2NO} \tag{3}$$

$$\frac{m_{VO_2/AEG}}{m_{C-V_2NO}} = \frac{(I.t_D)_{C-V_2NO}}{(I.t_D)_{VO_2/AEG}} \tag{4}$$

where $m_{VO_2/AEG}$ and m_{V_2NO-C} are the mass loading of the positive and negative electrodes and $Q_{VO_2/AEG}$ and Q_{V_2NO-C} are the specific capacities of VO_2/AEG and C-V_2NO electrodes respectively and I is the current and t_D is the discharge time.

The ratio of discharge time of the VO_2/AEG and C-V_2NO composite at the same specific current is:

$$\frac{m_{VO_2/AEG}}{m_{C-V_2NO}} = 0.68 \quad (5)$$

From equations 4, the masses loading of VO_2/AEG and C-V_2NO electrodes were calculated to be approximatively 2.2 and 3.3 mg respectively, which indicates a total mass of the asymmetric device to be 5.5 mg.

Fig. 9(a) shows the CV curves of the VO_2/AEG and C-V_2NO electrodes as evaluated in half-cell configuration with working potential windows of 0.0 to 0.5 V and −1.2 to 0.0 V, respectively at a scan rate of 50 mV s^{-1}. Fig. 9(b) shows the CV curves of the asymmetric device at different scan rates from 5 to 500 mV s^{-1}. For instance, at a scan rate of 50 mV s^{-1}, the CV curve of the device showed a pair of redox peaks corresponding to the anodic peak at ~ 0.94 V and cathodic peak at ~1.45 V. The CV curves obtained of the device show faradaic type behavior at different scan rates in the potential range of 0.0 V to 1.8 V. As observed, the CV curves response have a similar shape with increasing scan rate from 5 to 500 mV s^{-1}, showing good efficient electron transfer in the electrodes and a superb rate capability.

Fig. 9(b) also exhibits a low positive shift of the anodic peaks (oxidation) and a low negative shift of the cathodic peaks (reduction) which indicated a quasi-reversible nature of the redox reactions [86].

Fig. 9(c) shows the GCD curves of VO_2/AEG//C-V_2NO at different gravimetric current values of 1 - 20 A g^{-1} in a 0.0 to 1.8 V cell potential. The GCD curves are clearly non-linear which confirms the faradic behavior of the asymmetric device.

From the GCD curves, the specific capacity Q (mA h g^{-1}) of the VO_2/AEG//C-V_2NO was calculated using equation (2). The plot of the specific capacity as a function of the specific current is shown in Fig. 9(d). The device specific capacity reached a value of 46 mA h g^{-1} at a current density of 1 A g^{-1} and is maintained at 11 mA h g^{-1} at a 20 A g^{-1} gravimetric current.

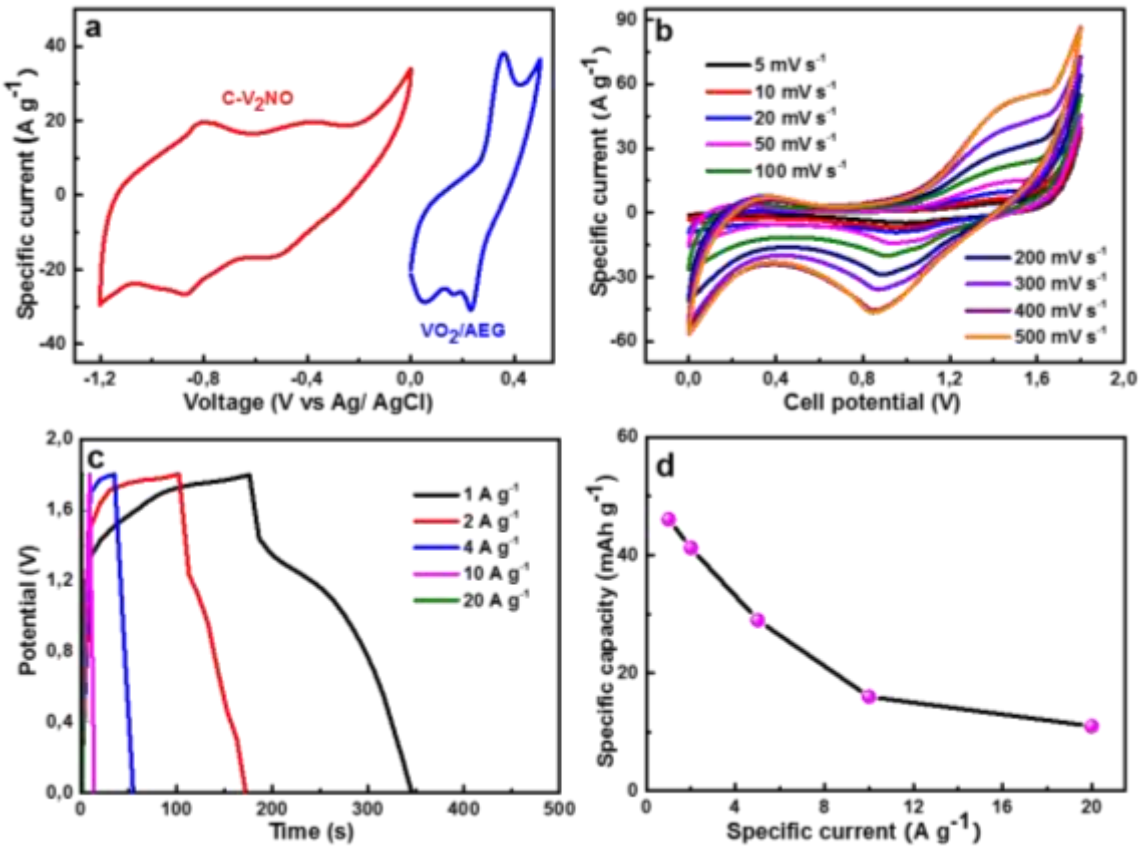

Fig. 9: (a) CV of VO_2/AEG and C-V_2NO in the positive and negative potential windows respectively, at 50 mV s^{-1} for half-cell configuration, (b) CV curves at different scan rates, (c) GCD profile at different specific currents and (d) specific capacity at different specific current of the AsyCs in the full-cell configuration.

The specific energy E_d (W h kg^{-1}) and specific power, P_d (W kg^{-1}) of the VO_2/AEG//C-V_2NO were also evaluated at different specific current values using equations (6) and (7) below:

$$E_d\,(\mathrm{W\,h\,kg^{-1}}) = \frac{I_d}{3.6}\int V(t)dt \tag{6}$$

$$P_d\,(\mathrm{W\,kg^{-1}}) = 3600\,\frac{E_D}{t_D} \tag{7}$$

where I_d is the specific current in A g^{-1}, t_D is the discharge time (s), and V is the potential window (V) of the asymmetric device.

The Ragone plot for the asymmetric device at different specific currents is shown in Fig. 10(a). A specific energy of 41.6 Wh kg^{-1} was recorded for the VO_2/AEG//C-V_2NO device with a corresponding specific power value of 904 W kg^{-1} at a specific current of 1 A g^{-1}.

At a high specific current of 20 A g^{-1}, an 18 kW kg^{-1} specific power was measured for the device with a correspond 9 W h kg^{-1} of specific energy. In addition, the specific energy and specific power values are higher than those reported for most reports on VO_2 and other VO_2/carbon-based composite materials as shown in the figure [39,42,87].

For example, Deng *et al.* [42] synthesized a graphene/VO_2 (RG/VO_2) composite by using a hydrothermal method with ammonium metavanadate (NH_4VO_3), formic acid and graphite oxide (GO) nanosheets as precursors. Asymmetric device assembled using the RG/VO_2 as a positive and RG as a negative electrodes respectively in 0.5 M K_2SO_4 electrolyte. The specific energy of the RG/VO_2//RG was 22.8 Wh kg^{-1} with a specific power of 425 W kg^{-1} at a specific current of 0.5 A g^{-1} [42]. Wang and co-authors [39] prepared a 3D graphene/VO_2 nanobelt composite hydrogel using a commercial vanadium pentoxide (V_2O_5) and graphene oxide as precursors. The symmetric capacitors delivered a specific energy of 21.3 W h kg^{-1} with a specific power ~ 304 W kg^{-1} at a specific current of 1 A g^{-1} in 0.5 M K_2SO_4 [39]. Ma and co-workers [87] reported a 3D VO_2 irregular ellipsoidal material using a simple CVD method with ammonium metavanadate (NH_4VO_3) as a precursor. The electrochemical performance of the symmetric device (VO_2//VO_2) exhibited specific energy of 21.3 W h kg^{-1} with a specific power of 207.2 W kg^{-1} at a specific current of 0.25 A g^{-1} in 1M Na_2SO_4 [87]. The high specific energy and specific power of the VO_2/AEG//C-V_2NO asymmetric device which are superior to similar devices, reported in this work are associated with the good electrochemical performances of both electrodes and the large working potential. It can also be related to the fast kinetics of charge/discharge process and the high ionic conductivity of the electrolyte ions [88].

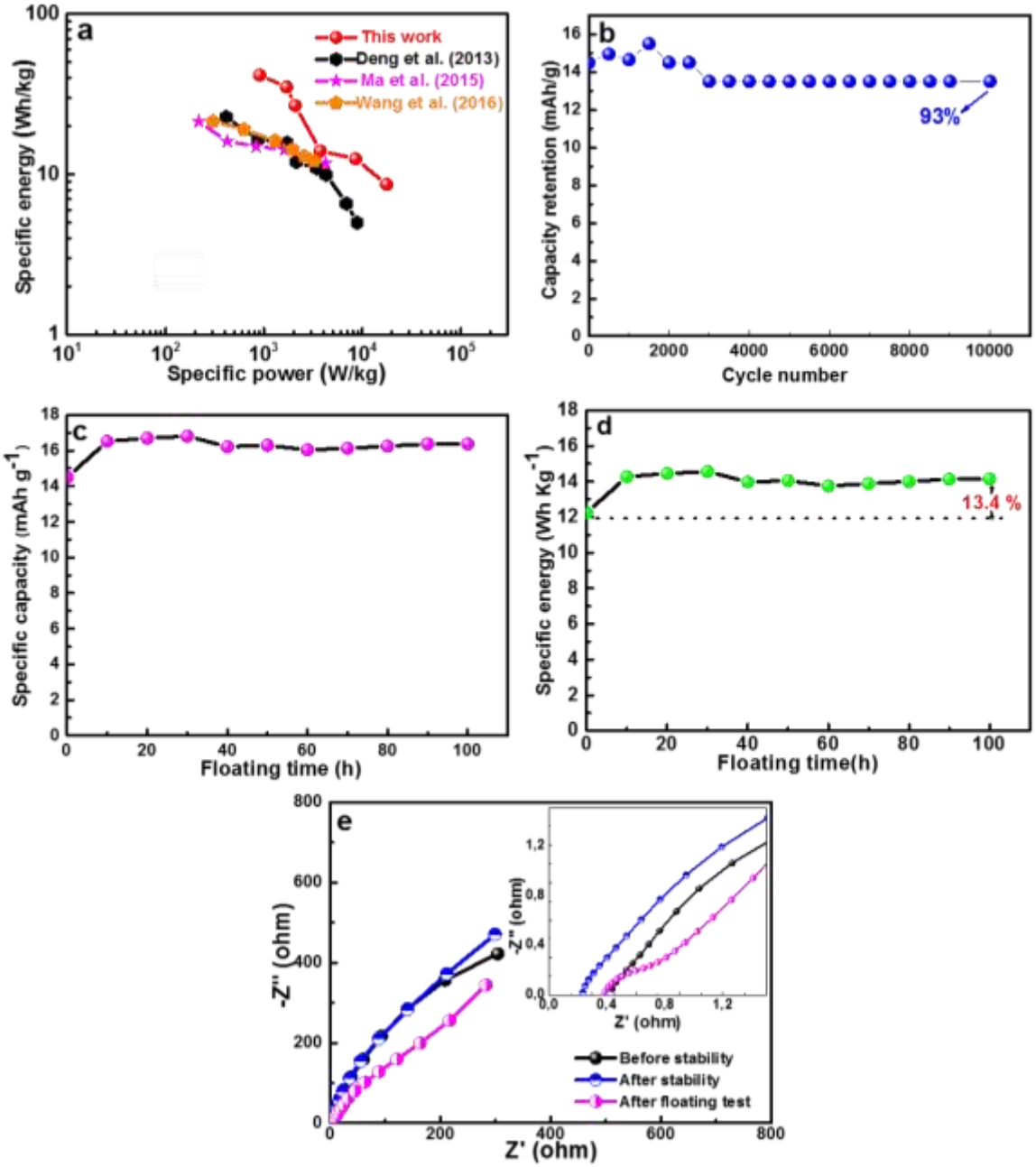

Fig. 10: (a) Ragone plot of the specific power as a function of specific energy, (b) stability test showing capacity retention for up to 10,000 cycles, (c) plot of specific capacity, (d) plot of specific energy versus floating time to 100 h at 10 A g^{-1} and (e) Nyquist plot (the inset is the ESR) of the asymmetric device before, after the stability and after floating test.

In order to evaluate the stability of the VO_2/AEG//C-V_2NO, the asymmetric device was exposed to 10,000 constant charge-discharge cycles at a specific current of 10 A g^{-1}.

Such a test is an essential parameter if the device is to be considered for practical application in a supercapacitor. The plot of capacity retention as a function of cycle number at 10 A g^{-1} is shown in Fig. 10(b) in a wide operating voltage of 1.8 V. An unstable capacity retention is

initially observed for the first 2500 cycles due to mechanical stress [89] before stabilizing. However, above 2500 cycles, an excellent capacity retention of 93% is obtained up to 10,000th charge-discharge cycle. This indicates an excellent electrochemical stability of the electrode material. The good stability test is linked to the incorporation of VO_2 rods within the AEG sheet-like material (positive electrode) as well as the use of a porous web-like C-V_2NO nanostructure (negative electrode).

Actually, high specific energy, high specific power, and good stability are critical for a good electrochemical capacitor. The additional stability test was also studied using the floating test (also called voltage holding) after cycling. The floating test was designed to analyse the device specific capacity at each 10 h period of the potential holding step for up to 100 h. Fig. 10(c) shows a slow improvement in the device performance in terms of the specific capacity value after 30 h of floating before stabilizing at a constant value of 10 A g^{-1}. The good stability profile can be confirmed after evaluating the specific energy for each floating test as shown in Fig. 10(d) which presents the plot of specific energy as a function of floating time of 10 h interval. It shows an increase in the specific energy after 30 h which is in agreement with Fig. 10(c). The specific energy increased by 13.4% from the original value of 12.2 W h kg^{-1} which stabilizes to the same value up to 100 h (Fig. 10d). These increase in specific capacity and specific energy could be due to the increase in accessible redox sites during the aging time [59]. It also confirms that the VO_2/AEG//C-V_2NO device is stable with the cell voltage of 1.8 V by using 6 M KOH.

Fig. 10(e) shows the Nyquist plots of the asymmetric device before, after 10,000 cycling and after voltage holding carried out in the frequency range of 100 kHz to10 mHz. The ESR value of the device improved from 0.43 Ω before stability tests to 0.23 Ω after cycling test and 0.37 Ω after voltage holding respectively. The Nyquist plot after 10,000 cycling test shows a smaller deviation from the vertical line and shorter diffusion length as compared to others. This

continuous decrease of the ESR values after stability and after the maintenance of the voltage confirms the good accessible redox sites during the stability test.

3. Conclusion

In this work, the VO_2/AEG rod-like composite and porous C-V_2NO with a spider web-like structure were successfully synthesized by CVD method. The powder X-ray diffraction analysis of the VO_2/AEG composite showed the diffraction peaks of the VO_2 and AEG while for C-V_2NO, it shows a cubic crystal structure. The electrochemical performance of the electrode materials (VO_2/AEG// C-V_2NO) was evaluated in a two-electrode asymmetric device with VO_2/AEG composite as a positive and C-V_2NO as a negative electrodes respectively in a 6 M KOH. The VO_2/AEG//C-V_2NO exhibited a specific energy of 41.6 Wh kg^{-1} associated with a specific power of 904 W kg^{-1} at a specific current of 1 A g^{-1} in a large operating voltage of 1.8 V. These values supersede the recorded values reported in for VO_2 based devices.

The asymmetric supercapacitor showed an excellent capacity retention of 93% for up to 10,000 cycling test at a specific current of 10 A g^{-1}. It also showed good stability through floating test up to 100 h exhibiting a high specific energy which revealed that the electrode materials showed better-performance after voltage holding measurements. The results confirmed that the VO_2/AEG composite and C-V_2NO materials are suitable for high performance asymmetric capacitor applications.

Acknowledgment

This research was supported by the South African Research Chairs Initiative (SARChI) of the Department of Science and Technology (DST) through the National Research Foundation (NRF) of South Africa (Grant No. 61056). Any idea, finding, conclusion or recommendation expressed in this material is that of the author(s). The NRF does not accept any liability in this regard. N. M. Ndiaye thanks Dr. Bridget K. Mutuma for discussions on the morphological

properties and the fitting of XPS. N. M. Ndiaye thanks 'Organization for Women in Science for the Developing World (OWSD) and Swedish International Development Cooperation Agency (Sida), NRF through SARChI in Carbon Technology and Materials and the University of Pretoria for financial support.

References

[1] Y. Zhang, J. Zheng, T. Hu, F. Tian, C. Meng, Synthesis and supercapacitor electrode of VO_2(B)/C core–shell composites with a pseudocapacitance in aqueous solution, Applied Surface Science. 371 (2016) 189–195. doi:10.1016/J.APSUSC.2016.02.199.

[2] M. Vangari, T. Pryor, L. Jiang, Supercapacitors: Review of Materials and Fabrication Methods, Journal of Energy Engineering. 139 (2013) 72–79. doi:10.1061/(ASCE)EY.1943-7897.0000102.

[3] M. Gidwani, A. Bhagwani, N. Rohra, Supercapacitors: the near Future of Batteries, International Journal of Engineering Inventions. 4 (2014) 22–27. www.ijeijournal.com (accessed October 1, 2018).

[4] R.B. Rakhi, D.H. Nagaraju, P. Beaujuge, H.N. Alshareef, Supercapacitors based on two dimensional VO_2 nanosheet electrodes in organic gel electrolyte, Electrochimica Acta. 220 (2016) 601–608. doi:10.1016/J.ELECTACTA.2016.10.109.

[5] K.H. An, W.S. Kim, Y.S. Park, Y.C. Choi, S.M. Lee, D.C. Chung, D.J. Bae, S.C. Lim, Y.H. Lee, Supercapacitors Using Single-Walled Carbon Nanotube Electrodes, Advanced Materials. 13 (2001) 497–500. doi:10.1002/1521-4095(200104)13:7<497::AID-ADMA497>3.0.CO;2-H.

[6] J.R. Miller, R.A. Outlaw, B.C. Holloway, K.J. Ganesh, W. Cai, P.J. Ferreira, A. Pirkle, R.M. Wallace, K.A. Cychosz, M. Thommes, D. Su, E.A. Stach, R.S. Ruoff, Graphene Double-Layer Capacitor with ac Line-Filtering Performance, Science. 329 (2010) 1637–1639. doi:10.1126/science.1194372.

[7] Z. Yu, L. Tetard, L. Zhai, J. Thomas, Supercapacitor electrode materials: nanostructures from 0 to 3 dimensions, Energy Environ. Sci. 8 (2015) 702–730. doi:10.1039/C4EE03229B.

[8] X. Pan, Y. Zhao, G. Ren, Z. Fan, Highly conductive VO2 treated with hydrogen for supercapacitors, Chemical Communications. 49 (2013) 3943. doi:10.1039/c3cc00044c.

[9] M. Winter, R.J. Brodd, What Are Batteries, Fuel Cells, and Supercapacitors?, Chem. Rev. 104 (2004) 4245−4269. doi:10.1021/CR020730K.

[10] M. Zhi, C. Xiang, J. Li, M. Li, N. Wu, Nanostructured carbon–metal oxide composite electrodes for supercapacitors: a review, Nanoscale. 5 (2013) 72–88. doi:10.1039/C2NR32040A.

[11] J.-W. Lang, L.-B. Kong, W.-J. Wu, Y.-C. Luo, L. Kang, Facile approach to prepare loose-packed NiO nano-flakes materials for supercapacitors, Chemical Communications. 104 (2008) 4213. doi:10.1039/b800264a.

[12] H. Li, Y. Gao, C. Wang, G. Yang, A simple electrochemical route to access amorphous mixed-metal hydroxides for supercapacitor electrode materials, Advanced Energy Materials. 5 (2015) 1401767. doi:10.1002/aenm.201401767.

[13] H. Xu, X. Hu, H. Yang, Y. Sun, C. Hu, Y. Huang, Flexible Asymmetric Micro-Supercapacitors Based on Bi_2O_3 and MnO_2 Nanoflowers: Larger Areal Mass Promises Higher Energy Density, Advanced Energy Materials. 5 (2015) 1401882. doi:10.1002/aenm.201401882.

[14] H. Ma, J. He, D.-B. Xiong, J. Wu, Q. Li, V. Dravid, Y. Zhao, Nickel Cobalt Hydroxide @Reduced Graphene Oxide Hybrid Nanolayers for High Performance Asymmetric Supercapacitors with Remarkable Cycling Stability, ACS Applied Materials & Interfaces. 8 (2016) 1992–2000. doi:10.1021/acsami.5b10280.

[15] G.A. Snook, P. Kao, A.S. Best, Conducting-polymer-based supercapacitor devices and electrodes, Journal of Power Sources. 196 (2011) 1–12. doi:10.1016/J.JPOWSOUR.2010.06.084.

[16] A. Rudge, J. Davey, I. Raistrick, S. Gottesfeld, J.P. Ferraris, Conducting polymers as active materials in electrochemical capacitors, Journal of Power Sources. 47 (1994) 89–107. doi:10.1016/0378-7753(94)80053-7.

[17] X. Wang, A. Sumboja, M. Lin, J. Yan, P.S. Lee, Enhancing electrochemical reaction sites in nickel–cobalt layered double hydroxides on zinc tin oxide nanowires: a hybrid material for an asymmetric supercapacitor device, Nanoscale. 4 (2012) 7266. doi:10.1039/c2nr31590d.

[18] L.-B. Kong, M. Liu, J.-W. Lang, Y.-C. Luo, L. Kang, Asymmetric Supercapacitor Based on Loose-Packed Cobalt Hydroxide Nanoflake Materials and Activated Carbon, Journal of The Electrochemical Society. 156 (2009) A1000. doi:10.1149/1.3236500.

[19] H. Wang, H. Yi, X. Chen, X. Wang, Asymmetric supercapacitors based on nano-architectured nickel oxide/graphene foam and hierarchical porous nitrogen-doped carbon nanotubes with ultrahigh-rate performance, J. Mater. Chem. A. 2 (2014) 3223–3230. doi:10.1039/C3TA15046A.

[20] J. Yan, Z. Fan, W. Sun, G. Ning, T. Wei, Q. Zhang, R. Zhang, L. Zhi, F. Wei, Advanced Asymmetric Supercapacitors Based on Ni(OH)2/Graphene and Porous Graphene Electrodes with High Energy Density, Advanced Functional Materials. 22 (2012) 2632–2641. doi:10.1002/adfm.201102839.

[21] Z.-S. Wu, W. Ren, D.-W. Wang, F. Li, B. Liu, H.-M. Cheng, High-Energy MnO_2 Nanowire/Graphene and Graphene Asymmetric Electrochemical Capacitors, ACS Nano. 4 (2010) 5835–5842. doi:10.1021/nn101754k.

[22] C.M. Ghimbeu, E. Raymundo-Piñero, P. Fioux, F.F. Béguin, C. Vix-Guterl, Vanadium nitride/carbon nanotube nanocomposites as electrodes for supercapacitors, Journal of Materials Chemistry. 21 (2011) 13268. doi:10.1039/c1jm11014d.

[23] R.L. Porto, R. Frappier, J.B.B. Ducros, C. Aucher, H. Mosqueda, S. Chenu, B. Chavillon, F. Tessier, F. Cheviré, T. Brousse, Titanium and vanadium oxynitride powders as pseudo-capacitive materials for electrochemical capacitors, in: Electrochimica Acta, Pergamon, 82 (2012) 257–262. doi:10.1016/J.ELECTACTA.2012.05.032.

[24] E. Eustache, R. Frappier, R.L. Porto, S. Bouhtiyya, J.-F. Pierson, T. Brousse, Asymmetric electrochemical capacitor microdevice designed with vanadium nitride and nickel oxide thin film electrodes, Electrochemistry Communications. 28 (2013) 104–106. doi:10.1016/J.ELECOM.2012.12.015.

[25] L. Zhang, F. Zhang, X. Yang, G. Long, Y. Wu, T. Zhang, K. Leng, Y. Huang, Y. Ma, A. Yu, Y. Chen, Porous 3D graphene-based bulk materials with exceptional high surface area and excellent conductivity for supercapacitors, Scientific Reports. 3 (2013) 1408. doi:10.1038/srep01408.

[26] L.L. Zhang, X.S. Zhao, Carbon-based materials as supercapacitor electrodes, Chemical Society Reviews. 38 (2009) 2520. doi:10.1039/b813846j.

[27] C. Peng, S. Zhang, D. Jewell, G.Z. Chen, Carbon nanotube and conducting polymer composites for supercapacitors, Progress in Natural Science. 18 (2008) 777–788. doi:10.1016/J.PNSC.2008.03.002.

[28] Z. Fan, J. Yan, T. Wei, L. Zhi, G. Ning, T. Li, F. Wei, Asymmetric Supercapacitors Based on Graphene/MnO_2 and Activated Carbon Nanofiber Electrodes with High Power and Energy Density, Advanced Functional Materials. 21 (2011) 2366–2375. doi:10.1002/adfm.201100058.

[29] H. Zhao, L. Pan, S. Xing, J. Luo, J. Xu, Vanadium oxides–reduced graphene oxide composite for lithium-ion batteries and supercapacitors with improved electrochemical performance, Journal of Power Sources. 222 (2013) 21–31. doi:10.1016/j.jpowsour.2012.08.036.

[30] X. Pan, G. Ren, M.N.F. Hoque, S. Bayne, K. Zhu, Z. Fan, Fast Supercapacitors Based on Graphene-Bridged V_2O_3/VO_x Core-Shell Nanostructure Electrodes with a Power Density of 1 MW kg $^{-1}$, Advanced Materials Interfaces. 1 (2014) 1400398. doi:10.1002/admi.201400398.

[31] W.F. Mak, G. Wee, V. Aravindan, N. Gupta, S.G. Mhaisalkar, S. Madhavi, High-Energy Density Asymmetric Supercapacitor Based on Electrospun Vanadium Pentoxide and Polyaniline Nanofibers in Aqueous Electrolyte, Journal of The Electrochemical Society. 159 (2012) A1481–A1488. doi:10.1149/2.040209jes.

[32] E. Umeshbabu, G. Ranga Rao, Vanadium pentoxide nanochains for high-performance electrochemical supercapacitors, Journal of Colloid and Interface Science. 472 (2016) 210–219. doi:10.1016/j.jcis.2016.03.050.

[33] M.H. Bai, L.J. Bian, Y. Song, X.X. Liu, Electrochemical codeposition of vanadium oxide and polypyrrole for high-performance supercapacitor with high working voltage, ACS Applied Materials and Interfaces. 6 (2014) 12656–12664. doi:10.1021/am502630g.

[34] X. Pan, G. Ren, M.N.F. Hoque, S. Bayne, K. Zhu, Z. Fan, Fast supercapacitors based on graphene-bridged V_2O_3/VO_x core-shell nanostructure electrodes with a power density of 1 MW kg^{-1}, Advanced Materials Interfaces. 1 (2014) 1400398. doi:10.1002/admi.201400398.

[35] H. Li, K. Jiao, L. Wang, C. Wei, B. Xie, Micelle anchored in situ synthesis of V_2O_3 nanoflakes@C composites for supercapacitors, Journal of Materials Chemistry A: Materials for Energy and Sustainability. 2 (2014) 18806–18815. doi:10.1039/C4TA04062G.

[36] G.P. Nagabhushana, G.T. Chandrappa, Facile solution combustion synthesis of monoclinic VO_2: a unique and versatile approach, Journal of Materials Chemistry A. 1 (2013) 11539. doi:10.1039/c3ta11692a.

[37] I. Derkaoui, M. Khenfouch, I. Elmokri, S.J. Moloi, B.M. Mothudi, M.S. Dhlamini, M. Maaza, I. Zorkani, A. Jorio, Experimental Investigation of the Effect of Graphene Nanosheets on the Optical-Electrical Properties of Vanadium Oxide Nanocomposites, Graphene. 5 (2016) 14–24. doi:10.4236/graphene.2016.51002.

[38] S. Kachi, T. Takada, K. Kosuge, Electrical Conductivity of Vanadium Oxides, Journal of the Physical Society of Japan. 18 (1963) 1839–1840. doi:10.1143/JPSJ.18.1839.

[39] H. Wang, H. Yi, X. Chen, X. Wang, D.W. Liu, J. Liu, G.Z. Cao, P.M. Ajayan, F. Wei, One-step strategy to three-dimensional graphene/VO_2 nanobelt composite hydrogels for high performance supercapacitors, Journal of Materials Chemistry A. 2 (2014) 1165–1173. doi:10.1039/c3ta13932h.

[40] L. Liang, H. Liu, W. Yang, Fabrication of VO_2(B) hybrid with multiwalled carbon nanotubes to form a coaxial structure and its electrochemical capacitance performance, Journal of Alloys and Compounds. 559 (2013) 167–173. doi:10.1016/J.JALLCOM.2013.01.111.

[41] X. Xia, D. Chao, C.F. Ng, J. Lin, Z. Fan, H. Zhang, Z.X. Shen, H.J. Fan, VO_2 nanoflake arrays for supercapacitor and Li-ion battery electrodes: performance enhancement by hydrogen molybdenum bronze as an efficient shell material, Mater. Horiz. 2 (2015) 237–244. doi:10.1039/C4MH00212A.

[42] L. Deng, G. Zhang, L. Kang, Z. Lei, C. Liu, Z.-H.H. Liu, Graphene/VO_2 hybrid material for high performance electrochemical capacitor, Electrochimica Acta. 112 (2013) 448–457. doi:10.1016/j.electacta.2013.08.158.

[43] G. Nie, X. Lu, Y. Zhu, M. Chi, M. Gao, S. Chen, C. Wang, Reactive Template Synthesis of Inorganic/Organic VO_2@Polyaniline Coaxial Nanobelts for High-Performance Supercapacitors, ChemElectroChem. 4 (2017) 1095–1100. doi:10.1002/celc.201600830.

[44] Z. Chen, V. Augustyn, J. Wen, Y. Zhang, M. Shen, B. Dunn, Y. Lu, High-Performance Supercapacitors Based on Intertwined CNT/V_2O_5 Nanowire Nanocomposites, Advanced Materials. 23 (2011) 791–795. doi:10.1002/adma.201003658.

[45] X. Zhou, Q. Chen, A. Wang, J. Xu, S. Wu, J. Shen, Bamboo-like Composites of V_2O_5/Polyindole and Activated Carbon Cloth as Electrodes for All-Solid-State Flexible Asymmetric Supercapacitors, ACS Applied Materials & Interfaces. 8 (2016) 3776–3783. doi:10.1021/acsami.5b10196.

[46] S. Fleischmann, M. Zeiger, N.J. Ackel, B. Krüner, K. Krüner, V. Lemkova, M. Widmaier, V. Presser, Tuning pseudocapacitive and battery-like lithium intercalation in vanadium dioxide/carbon onion hybrids for asymmetric supercapacitor anodes, (2017). doi:10.1039/c7ta02564e.

[47] H. Hosseini, S. Shahrokhian, Vanadium dioxide-anchored porous carbon nanofibers as a Na^+ intercalation pseudocapacitance material for development of flexible and super light electrochemical energy storage systems, Applied Materials Today. 10 (2018) 72–85. doi:10.1016/J.APMT.2017.11.011.

[48] F. Barzegar, A. Bello, D. Momodu, M.J. Madito, J. Dangbegnon, N. Manyala, Preparation and characterization of porous carbon from expanded graphite for high energy density supercapacitor in aqueous electrolyte, Journal of Power Sources. 309 (2016) 245–253. doi:10.1016/J.JPOWSOUR.2016.01.097.

[49] X.-J.J. Ma, W.-B. Bin Zhang, L.-B. Bin Kong, Y.-C.C. Luo, L. Kang, VO_2: from negative electrode material to symmetric electrochemical capacitor, RSC Advances. 5 (2015) 97239–97247. doi:10.1039/C5RA18758C.

[50] S. Lee, I.N. Ivanov, J.K. Keum, H.N. Lee, Epitaxial stabilization and phase instability of VO_2 polymorphs, Scientific Reports. 6 (2016) 19621. doi:10.1038/srep19621.

[51] N.M.M. Ndiaye, T.M.M. Masikhwa, B.D.D. Ngom, M.J.J. Madito, K.O.O. Oyedotun, J.K.K. Dangbegnon, N. Manyala, Effect of growth time on solvothermal synthesis of vanadium dioxide for electrochemical supercapacitor application, Materials Chemistry and Physics. 214 (2018) 192–200. doi:10.1016/j.matchemphys.2018.04.087.

[52] M. Pan, J. Liu, H. Zhong, S. Wang, Z.F. Li, X. Chen, W. Lu, Raman study of the phase transition in VO_2 thin films, Journal of Crystal Growth. 268 (2004) 178–183. doi:10.1016/j.jcrysgro.2004.05.005.

[53] G.I. Petrov, V.V. Yakovlev, J. Squier, Raman microscopy analysis of phase transformation mechanisms in vanadium dioxide, Applied Physics Letters. 81 (2002) 1023–1025. doi:10.1063/1.1496506.

[54] M. Lee, S.K. Balasingam, H.Y. Jeong, W.G. Hong, H.-B.-R. Lee, B.H. Kim, Y. Jun, One-step hydrothermal synthesis of graphene decorated V_2O_5 nanobelts for enhanced electrochemical energy storage, Scientific Reports. 5 (2015) 8151. doi:10.1038/srep08151.

[55] M. Chhowalla, A.C. Ferrari, J. Robertson, G.A.J. Amaratunga, Evolution of sp^2 bonding with deposition temperature in tetrahedral amorphous carbon studied by Raman spectroscopy, Applied Physics Letters. 76 (2000) 1419. doi:10.1063/1.126050.

[56] D. Roy, M. Chhowalla, H. Wang, N. Sano, I. Alexandrou, T.W. Clyne, G.A.J. Amaratunga, Characterisation of carbon nano-onions using Raman spectroscopy, Chemical Physics Letters. 373 (2003) 52–56. doi:10.1016/S0009-2614(03)00523-2.

[57] T.M.G. Mohiuddin, A. Lombardo, R.R. Nair, A. Bonetti, G. Savini, R. Jalil, N. Bonini, D.M. Basko, C. Galiotis, N. Marzari, K.S. Novoselov, A.K. Geim, A.C. Ferrari, Uniaxial strain in graphene by Raman spectroscopy: G peak splitting, Grüneisen parameters, and sample orientation, Physical Review B - Condensed Matter and Materials Physics. 79 (2009) 205433. doi:10.1103/PhysRevB.79.205433.

[58] S.-H. Lee, H.M. Cheong, M.J. Seong, P. Liu, C.E. Tracy, A. Mascarenhas, J.R. Pitts, S.K. Deb, Raman spectroscopic studies of amorphous vanadium oxide thin films, Solid State Ionics. 165 (2003) 111–116. doi:10.1016/j.ssi.2003.08.022.

[59] N.M. Ndiaye, B.D. Ngom, N.F. Sylla, T.M. Masikhwa, M.J. Madito, D. Momodu, T. Ntsoane, N. Manyala, Three dimensional vanadium pentoxide/graphene foam composite as positive electrode for high performance asymmetric electrochemical supercapacitor, Journal of Colloid and Interface Science. 532 (2018) 395–406. doi:10.1016/J.JCIS.2018.08.010.

[60] T.D. Manning, I.P. Parkin, C. Blackman, U. Qureshi, APCVD of thermochromic

vanadium dioxide thin films—solid solutions $V_{2-x}M_xO_2$ (M = Mo, Nb) or composites VO_2: SnO_2, Journal of Materials Chemistry. 15 (2005) 4560. doi:10.1039/b510552h.

[61] P. Schilbe, Raman scattering in VO_2, Physica B: Condensed Matter. 316–317 (2002) 600–602. doi:10.1016/S0921-4526(02)00584-7.

[62] A. Kafizas, G. Hyett, I.P. Parkin, Combinatorial atmospheric pressure chemical vapour deposition (cAPCVD) of a mixed vanadium oxide and vanadium oxynitride thin film, Journal of Materials Chemistry. 19 (2009) 1399. doi:10.1039/b817429f.

[63] M. Fabiane, M.J. Madito, A. Bello, N. Manyala, Raman spectroscopy and imaging of Bernal-stacked bilayer graphene synthesized on copper foil by chemical vapour deposition: growth dependence on temperature, Journal of Raman Spectroscopy. 48 (2017) 639–646. doi:10.1002/jrs.5094.

[64] J. Yu, G. Wang, B. Cheng, M. Zhou, Effects of hydrothermal temperature and time on the photocatalytic activity and microstructures of bimodal mesoporous TiO2 powders, Applied Catalysis B: Environmental. 69 (2007) 171–180. doi:10.1016/J.APCATB.2006.06.022.

[65] R.L. Porto, R. Frappier, J.B.B. Ducros, C. Aucher, H. Mosqueda, S. Chenu, B. Chavillon, F. Tessier, F. Cheviré, T. Brousse, Titanium and vanadium oxynitride powders as pseudo-capacitive materials for electrochemical capacitors, Electrochimica Acta. 82 (2012) 257–262. doi:10.1016/J.ELECTACTA.2012.05.032.

[66] D. Shu, H. Cheng, C. Lv, M.A. Asi, L. Long, C. He, X. Zou, Z. Kang, Soft-template synthesis of vanadium oxynitride-carbon nanomaterials for supercapacitors, International Journal of Hydrogen Energy. 39 (2014) 16139–16150. doi:10.1016/J.IJHYDENE.2014.05.119.

[67] F.O. Ochai-Ejeh, D.Y. Momodu, M.J. Madito, A.A. Khaleed, K.O. Oyedotun, S.C. Ray, N. Manyala, Nanostructured porous carbons with high rate cycling and floating performance for supercapacitor application, AIP Advances. 8 (2018) 055208. doi:10.1063/1.5023046.

[68] D. Verma, D. Singh, P. Kumar, P. Avasthi, V. Balakrishnan, Gram scale synthesis of monoclinic VO_2 microcrystals by hydrothermal and argon annealing treatment, Ceramics International. 45 (2019) 3554–3562. doi:10.1016/J.CERAMINT.2018.11.014.

[69] C. Cao, Y. Gao, H. Luo, Pure Single-Crystal Rutile Vanadium Dioxide Powders: Synthesis, Mechanism and Phase-Transformation Property, The Journal of Physical Chemistry C. 112 (2008) 18810–18814. doi:10.1021/jp8073688.

[70] Z. Huang, H. Zeng, L. Xue, X. Zhou, Y. Zhao, Q. Lai, Synthesis of vanadium oxide, V6O13 hollow-flowers materials and their application in electrochemical supercapacitors, Journal of Alloys and Compounds. 509 (2011) 10080–10085. doi:10.1016/J.JALLCOM.2011.08.042.

[71] M. Demeter, M. Neumann, W. Reichelt, Mixed-valence vanadium oxides studied by XPS, Surface Science. 454–456 (2000) 41–44. doi:10.1016/S0039-6028(00)00111-4.

[72] E. Hryha, E. Rutqvist, L. Nyborg, Stoichiometric vanadium oxides studied by XPS, Surface and Interface Analysis. 44 (2012) 1022–1025. doi:10.1002/sia.3844.

[73] G. Silversmit, D. Depla, H. Poelman, G.B. Marin, R. De Gryse, Determination of the V2p XPS binding energies for different vanadium oxidation states (V^{5+} to V^{0+}), Journal

of Electron Spectroscopy and Related Phenomena. 135 (2004) 167–175. doi:10.1016/J.ELSPEC.2004.03.004.

[74] D. Marton, K.J. Boyd, A.H. Al-Bayati, S.S. Todorov, J.W. Rabalais, Carbon nitride deposited using energetic species: A two-phase system, Physical Review Letters. 73 (1994) 118–121. doi:10.1103/PhysRevLett.73.118.

[75] M. Sevilla, A.B. Fuertes, The production of carbon materials by hydrothermal carbonization of cellulose, Carbon. 47 (2009) 2281–2289. doi:10.1016/j.carbon.2009.04.026.

[76] J.G.G. Chen, C.M.M. Kirn, B. Frühberger, B.D.D. DeVries, M.S.S. Touvelle, A NEXAFS determination of the oxidation state of vanadium carbide on V(110): observation of charge transfer from vanadium to carbon, Surface Science. 321 (1994) 145–155. doi:10.1016/0039-6028(94)90035-3.

[77] X. Song, D. Gopireddy, C.G. Takoudis, Characterization of titanium oxynitride films deposited by low pressure chemical vapor deposition using amide Ti precursor, Thin Solid Films. 516 (2008) 6330–6335. doi:10.1016/J.TSF.2007.12.148.

[78] P. Mérel, M. Tabbal, M. Chaker, S. Moisa, J. Margot, Direct evaluation of the sp^3 content in diamond-like-carbon films by XPS, Applied Surface Science. 136 (1998) 105–110. doi:10.1016/S0169-4332(98)00319-5.

[79] A. Dementjev, A. de Graaf, M.C. van de Sanden, K. Maslakov, A. Naumkin, A. Serov, X-Ray photoelectron spectroscopy reference data for identification of the C_3N_4 phase in carbon–nitrogen films, Diamond and Related Materials. 9 (2000) 1904–1907. doi:10.1016/S0925-9635(00)00345-9.

[80] M. Fredriksson, C. Langhammer, Electrochemical hydride formation in thin Pd films analyzed with a combined optical and electrochem-ical technique, Chalmers University of Technology, 2014. http://publications.lib.chalmers.se/records/fulltext/209369/209369.pdf (accessed April 25, 2019).

[81] C.H. Hamann, A. Hamnett, W. Vielstich, Electrochemistry, Wiley-VCH, 2007. https://www.wiley.com/en-za/Electrochemistry,2nd, Completely Revised and Updated Edition-p-9783527310692 (accessed April 25, 2019).

[82] S. Leijonmarck, Preparation and Characterization of Electrochemical Devices for Energy Storage and Debonding, School of Chemical Science and Engineering Kungliga Tekniska Högskolan, 2013. https://www.diva-portal.org/smash/get/diva2:613847/FULLTEXT01.pdf (accessed April 25, 2019).

[83] Y.-G. Wang, L. Cheng, Y.-Y. Xia, Electrochemical profile of nano-particle CoAl double hydroxide/active carbon supercapacitor using KOH electrolyte solution, Journal of Power Sources. 153 (2006) 191–196. doi:10.1016/j.jpowsour.2005.04.009.

[84] H. Bin Wu, H. Pang, X.W. (David) Lou, Facile synthesis of mesoporous $Ni_{0.3}Co_{2.7}O_4$ hierarchical structures for high-performance supercapacitors, Energy & Environmental Science. 6 (2013) 3619. doi:10.1039/c3ee42101e.

[85] M.M. Shaijumon, F.S. Ou, L. Ci, P.M. Ajayan, Synthesis of hybrid nanowire arrays and their application as high power supercapacitor electrodes, Chemical Communications. 0 (2008) 2373. doi:10.1039/b800866c.

[86] Y.-K. Hsu, Y.-C. Chen, Y.-G. Lin, Synthesis of copper sulfide nanowire arrays for high-performance supercapacitors, Electrochimica Acta. 139 (2014) 401–407. doi:10.1016/J.ELECTACTA.2014.06.138.

[87] X.-J. Ma, W.-B. Zhang, L.-B. Kong, Y.-C. Luo, L. Kang, VO_2: from negative electrode material to symmetric electrochemical capacitor, RSC Advances. 5 (2015) 97239–97247. doi:10.1039/C5RA18758C.

[88] A. Leela Mohana Reddy, F. Estaline Amitha, I. Jafri, S. Ramaprabhu, Asymmetric flexible supercapacitor stack, Nanoscale Research Letters. 3 (2008) 145–151. doi:10.1007/s11671-008-9127-3.

[89] B. Saravanakumar, K.K. Purushothaman, G. Muralidharan, Interconnected V_2O_5 Nanoporous Network for High-Performance Supercapacitors, ACS Applied Materials & Interfaces. 4 (2012) 4484–4490. doi:10.1021/am301162p.